



Significant enhanced performance for Rhodamine B, phenol and Cr(VI) removal by Bi₂WO₆ nanocomposites via reduced graphene oxide modification

Hongwei Ma, Jianfeng Shen, Min Shi, Xin Lu, Zhiqiang Li, Yu Long, Na Li, Mingxin Ye*

Center of Special Materials and Technology, Fudan University, Shanghai 200433, China

ARTICLE INFO

Article history:

Received 7 December 2011

Received in revised form 7 March 2012

Accepted 27 March 2012

Available online 2 April 2012

Keywords:

Reduced graphene oxide

Hydrothermal

Bi₂WO₆

Degradation

Cr(VI) reduction

ABSTRACT

A series of reduced graphene oxide (RGO) modified Bi₂WO₆ nanocomposites were synthesized by hydrothermal method and characterized by X-ray diffraction, transmission electron microscopy, scanning electron microscopy, Raman spectroscopy and Brunauer–Emmett–Teller (BET) specific surface areas analysis. The results indicated that the RGO could be used as structure-directing agent in the process of formation of the RGO/Bi₂WO₆ nanocomposites. The as-prepared RGO/Bi₂WO₆ nanocomposites can effectively remove Rhodamine B, phenol and Cr(VI) from water under UV and visible light irradiation. Therefore, the amount of RGO in the composite is an important factor affecting photocatalytic activity of RGO/Bi₂WO₆ nanocomposites. Therefore, the optimum amount of RGO is 20 mg, at which the RGO/Bi₂WO₆ sample displays the highest reactivity. Furthermore, the as-prepared photocatalyst has its prominent potential as a readily separable and recoverable one. Our findings demonstrated that RGO could be utilized as a modified and structure-directing agent for promising development of high-performance photocatalysts in the environmental applications.

© 2012 Elsevier B.V. All rights reserved.

1. Introduction

Graphene, a new class of 2D carbonaceous material with atom-thick layer features, different from ball-like C₆₀ and 1D carbon nanotubes, has attracted much attention recently because it has many potential applications, such as in electronic, optical, and catalytic fields [1–4]. It can be obtained from micromechanical cleavage [5], thermal exfoliation [6,7], and chemical method [8] from bulk graphite. Among these methods, the chemical method is more convenient and makes the graphene oxide sheets are able to suspend in many solvents by introducing functional groups such as hydroxyl and carboxyl [9].

Metal tungstates, as one kind of multicomponent metal oxide compound, have received great interest over the past few years because of their potential applications in photoluminescence, microwave, optical fibers catalysts, magnetic devices and humidity sensors [10]. Bismuth tungstate (Bi₂WO₆, abbreviated as BW), one of the simplest Aurivillius phase oxides, has a layered structure in which the perovskite layer (WO₄)^{2–} lies between (Bi₂O₂)²⁺ layers [11]. It has attracted a great deal attention because of its excellent physical and chemical properties such as ferroelectric piezoelectricity, pyroelectricity, catalytic behavior, oxide anion conducting,

a nonlinear dielectric susceptibility, and luminescent properties [12–16]. Several methods have well been developed, such as electrospinning [17], hydrothermal treatment [18], sol–gel method [19] and microwave irradiation [11]. Namely, various morphologies of the BW have been fabricated, including flower-like [20,21], nest-like [22], hierarchical microsphere [23] and octahedron-like structures [24].

Recently, doping with suitable nonmetals has been attempted to improve the performances of the catalysts. For example, nitrogen [25], carbon [26], graphene [27], etc. have been used to modify BW materials. Among these methods, the graphene doping has been considered as a promising method to improve photocatalytic performances. Moreover, photocatalytic ability is closely related to the adsorptivity, conductivity, controllability, etc. of the photocatalyst [27]. Like single-walled carbon nanotubes, conducting/semiconducting fullerenes, graphene is also expected to be used as an efficient acceptor to enhance photoinduced charge transfer for improved catalytic activity [28–30]. This property of reduced graphene oxide (RGO) was utilized in our synthesis process, where a facile and simple route was demonstrated to obtain RGO/BW nanocomposites via hydrothermal reaction in the presence of the GO and sodium alginate (abbreviated as AL). Because of the unique properties of graphene, it not only improved the separation and transport of photocarriers, but also might cause a higher conduction band position with a stronger reductive power. Therefore, RGO/BW nanocomposites can remove Rhodamine B, phenol and Cr(VI) from water under UV and visible light irradiation.

* Corresponding author at: 220 Handan Road, Shanghai 200433, China.

Tel.: +86 021 55664095; fax: +86 021 55664094.

E-mail address: mxye@fudan.edu.cn (M. Ye).

Meanwhile, it was found that the photoactivity of the sample was strongly dependent on the amount of GO. The optimum amount of RGO is found to be 20 mg, at which the RGO/BW sample displays the highest reactivity. Our work may open up a new avenue toward the photocatalytic activity of BW and other hybrid nanomaterials, which can meet the growing demands for environmental purification from industrial effluents.

2. Experimental

2.1. Materials

Graphite flakes were purchased from Qingdao BCSM Co., Ltd. All the reagents were of analytical purity and were used as received from Shanghai Chemical Company and used without further purification. De-ionized water was used in all experiments.

2.2. Synthesis of GO

Graphene oxide was synthesized from graphite flakes by a modified Hummers method as presented elsewhere [8,31,32].

2.3. Synthesis of RGO/BW nanocomposite

In our work, RGO/BW nanostructures were synthesized by a one-step hydrothermal method under the assistance of the sodium alginate (AL). In a typical experiment, $\text{Na}_2\text{WO}_4 \cdot 2\text{H}_2\text{O}$ (1 mmol), $\text{Bi}(\text{NO}_3)_3 \cdot 6\text{H}_2\text{O}$ (1 mmol) and desired amount of GO (ultrasonication for 30 min dispersed in water) were added successively into 60 mL distilled water with strong stirring followed by 30 min ultrasonication, 10 mL AL (9 g/L) solution was added slowly. After being stirred for 3 h, the suspension was sealed into a Teflon-lined autoclave and maintained at 180°C for 16 h. Subsequently, the autoclave was cooled to room temperature naturally. The resulting samples were collected, washed with de-ionized water and dried at 60°C in air. The prepared products with different amounts of graphene oxide (20 mg, 30 mg and 50 mg) under the hydrothermal condition were denoted as the BW-X-AL, respectively (X is the amount of GO and AL is the sodium alginate, samples were denoted BW-20-AL, BW-30-AL and BW-50-AL correspondingly).

For a comparative study, keeping other conditions constant, pristine BW nanopowder was also synthesized in the absence of GO and AL under the hydrothermal condition (the sample denoted as BW). On the other hand, only in the presence of AL, the sample BW was prepared without the addition of GO (the sample was denoted as BW-AL).

2.4. Characterization

The morphologies of the products were characterized by scanning electron microscopy (SEM, JSM-6700) operated at an acceleration voltage of 10 kV. The crystalline structures of the products were analyzed by an X-ray diffractometer (XRD, Y-2000) with $\text{Cu K}\alpha$ radiation ($\lambda = 1.5418 \text{ \AA}$). Transmission electron microscopy (TEM) observations were carried out on a JEOL JEM-2010 instrument, UV-vis absorption spectra were on a Lambda 35 spectrophotometer in the wavelength range of 300–800 nm. Raman spectra were acquired with a Raman microspectrometer (Renishaw 1000 NR) using an Argon ion laser (514.5 nm). The BET surface areas of the samples were determined by nitrogen adsorption-desorption isotherm measurement at 77 K (Gemini 2360, Shimadzu). The UV-vis diffuse reflectance spectra were conducted on a UV-vis NIR spectrophotometer (Solidspec-FLS-920, Edinburgh) using an integrating-sphere accessory.

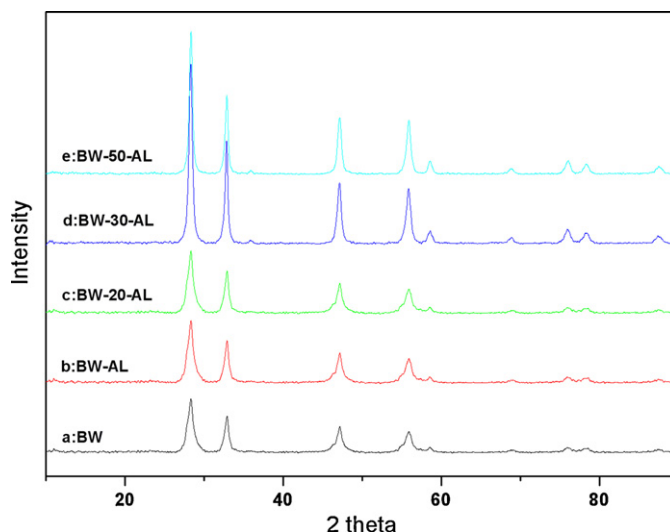


Fig. 1. XRD patterns of the (a) BW, (b) BW-AL, (c) BW-20-AL, (d) BW-30-AL, and (e) BW-50-AL samples.

3. Results and discussion

3.1. Crystal phase composition

Fig. 1 shows the XRD patterns of the samples prepared under different conditions. It was observed that the XRD patterns of the BW, BW-AL and BW-X-AL samples obtained under different conditions matched well with those of the orthorhombic BW sample (according to the JCPDS card no. 39-0256) [23,24] and all of the peaks could be indexed, as shown in Fig. 1. However, the diffraction peaks of RGO did not appear. We thought that both strong peaks of the BW and the low amount of RGO might be responsible for this phenomenon. The results were similar with previous reports [33].

3.2. Morphology

SEM and TEM images of the BW and RGO/BW samples obtained under different conditions are shown in Figs. 2a–e and 3a–d, respectively. It is observed that the BW samples fabricated under hydrothermal condition in the absence of the AL and GO displayed rectangle morphology with a length of $1 \mu\text{m}$ and width of 500 nm (Fig. 2a). In the absence of the GO and presence of the AL, however, the obtained BW-AL sample was composed of a large number of irregular nanosheets aggregations. On the other hand, in the presence of the AL and 20 mg GO, the GO was reduced to RGO by the AL under hydrothermal condition. The obtained sample BW-20-AL displayed flower-like spheres morphology. Some RGO sheets attached to the surface of the spheres (Fig. 3a and c). The results are different from the report [27], different morphology of the BW/graphene composite was obtained via a solvothermal route [27]. However, the BW-30-AL exhibited broken spheres morphology, when the GO amount rose to 30 mg. More RGO nanosheets could be observed on the surface of the spheres (Fig. 2d). Finally, the spheres completely collapsed when the GO amount was 50 mg. Therefore, the BW-50-AL sample displayed nanosheets morphology with about a length of $1 \mu\text{m}$ and width of 500 nm . This result demonstrated that RGO may act as a structure-directing agent (Figs. 3c and 2c). The more morphology information of the BW-X-AL samples could be shown in the Fig. Supplementary information (S1a–c). The EDX spectrum of BW-20-AL was shown in Fig. S1d. The EDX spectra indicated that the element Bi, W, O and C are observed in the products indicating the as-obtained product was RGO/BW nanocomposites. Moreover, more detail information

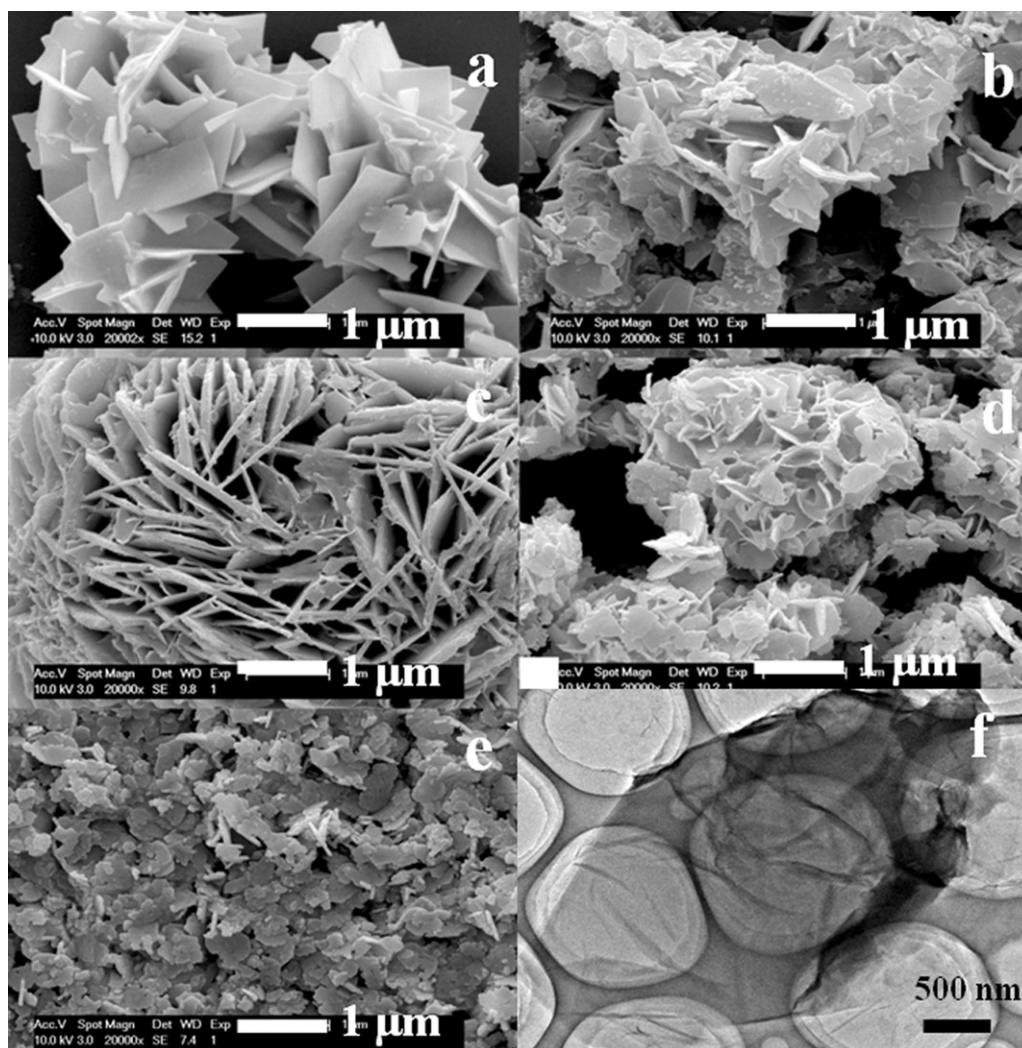


Fig. 2. SEM images of the (a) BW, (b) BW-AL, (c) BW-20-AL, (d) BW-30-AL and (e) BW-50-AL samples. (f) TEM images of the GO.

could be clearly seen from TEM images of the BW-20-AL and BW-50-AL samples. Fig. 3a clearly showed the sphere morphology of the BW-20-AL sample. From a magnified image (Fig. 3b), the particle size of the BW was estimated to be around 50 nm. The hybridization structures of BW and RGO sheets of the BW-50-AL sample was clearly observed in Fig. 3c and 3d. BW nanoparticles can interact with the graphene sheets through physisorption, electrostatic binding or through charge transfer interactions. The results were similar with previously reports [34–36]. TEM observation in Fig. 2f showed that GO nanosheets are highly transparent with folding at the edges, suggesting a very thin thickness. The RGO was prepared by the same hydrothermal method under the assistance of the AL. The corresponding SEM images are shown in Fig. S2. Above all, the RGO plays an important role in controlling over the morphologies of BW-X-AL nanostructured composites.

3.3. Raman spectra

Raman spectroscopy is a powerful nondestructive tool to characterize carbonaceous materials, particularly for ordered and disordered crystal structures of carbon. Fig. 4 indicates that several peaks in the range of 600–1000 cm^{-1} , which can be assigned to the stretches of the W–O bands [37]. In detail, the bands at 768 and 814 cm^{-1} are associated with antisymmetric and symmetric A_g modes of terminal O–W–O, respectively. The band at

307 cm^{-1} can be assigned to translational modes involving simultaneous motions of Bi^{3+} and WO_6^{6-} . The intensity of the peak at 727 cm^{-1} is interpreted as an antisymmetric bridging mode associated with the tungstate chain [9,25]. The Raman spectrum display two prominent peaks at around 1595 and 1346 cm^{-1} , which suggested that element C exists in the nanocomposites. The G band is usually assigned to the E_{2g} phonon of C sp^2 atoms, while the D band is a breathing mode of K-point phonons of A_{1g} symmetry. The Raman spectral results described above agree well with previous reports [38,39], indicating that the RGO in RGO-BW has been well deoxygenated and reduced to graphene. We know that the oxygen functional groups in GO sheets can be removed by chemical reduction, and the conjugated graphene network (sp^2 carbon) will be re-established.

3.4. Specific surface area analysis

Full nitrogen adsorption/desorption isotherms (left) and pore-size distribution curves (right) of the BW-X-AL samples are shown in Fig. 5. The curves of the products reveal that the three samples possess type III adsorption–desorption isotherms [40], which is caused by weak adsorbent–adsorbent interactions and the existence of the nanostructures in the sample. The BET specific surface areas of BW-20-AL, BW-30-AL and BW-50-AL were calculated to be 37, 23 and 19 m^2/g , respectively, suggesting that the optimum

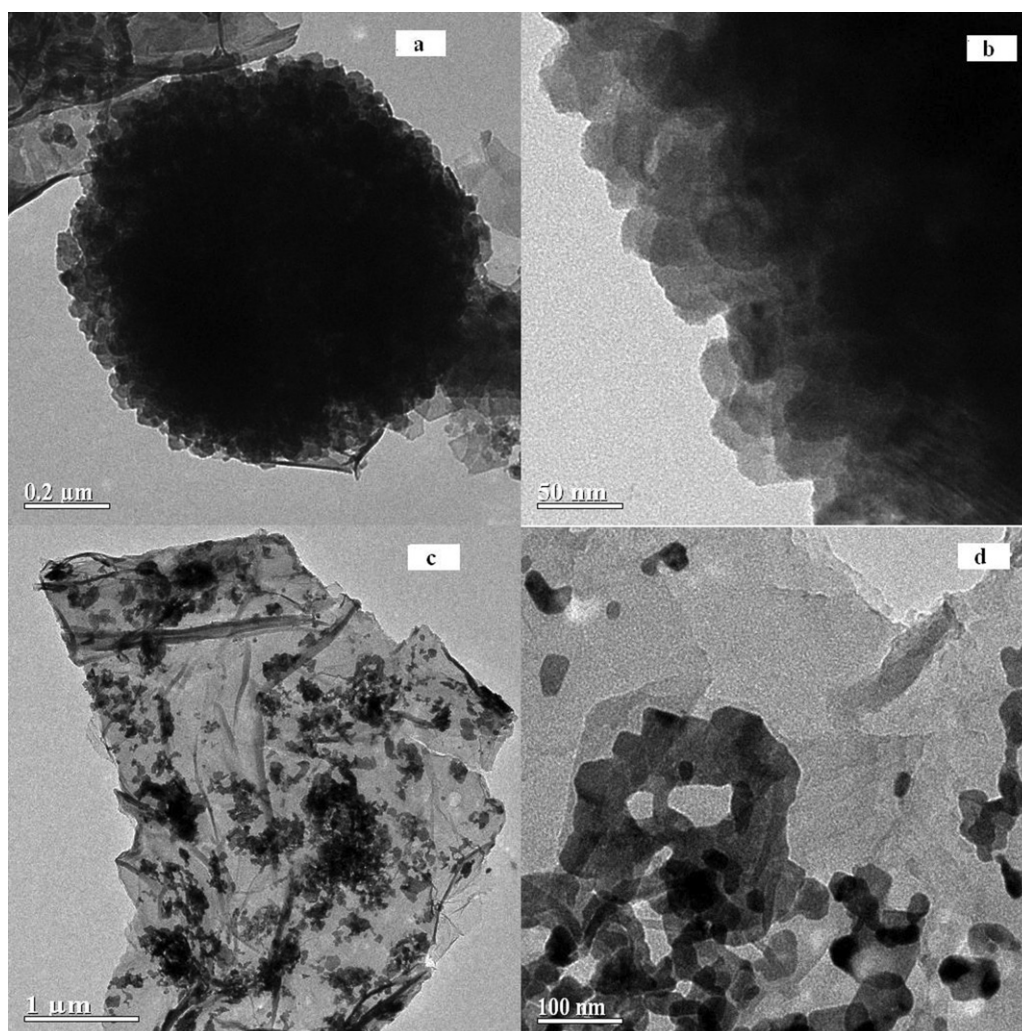


Fig. 3. TEM images of the samples (a and b): BW-20-AL; (c and d): BW-50-AL.

amount of RGO could significantly increase the surface area of the final product. On the other hand, this is attributed to the fact that the BW-20-AL possesses nanostructured spheres morphology. From the pore-size distribution curves of the samples, we could conclude that three samples possess a mean diameter around 2 nm. The different RGO content in the samples could be responsible for the slightly different pore size distributions. Therefore, more RGO sheets play an important role in the control over

morphology of the samples, including the different BET area and pore-size distribution.

3.5. UV-vis diffuse absorption spectra

The optical absorption properties of samples were measured by UV-vis spectrometry. From the typical diffuse absorption spectra of products (shown in Fig. S3), all samples display photoabsorption

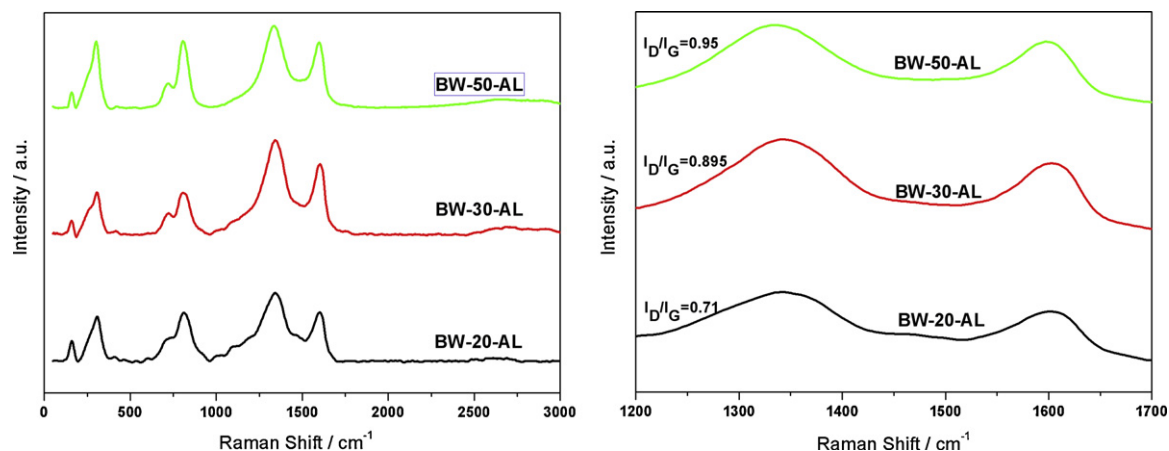


Fig. 4. Raman spectra of the BW-X-AL samples (left: full spectra, right: partial spectra).

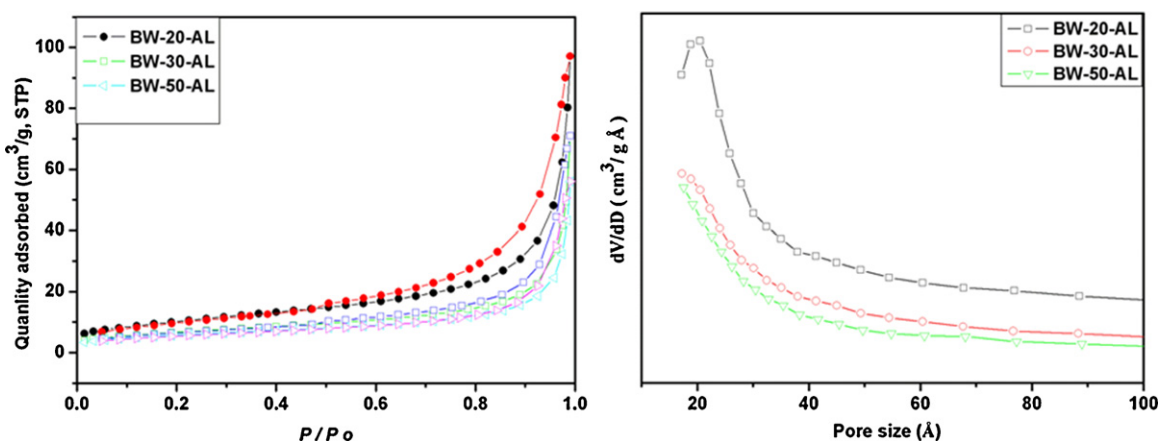


Fig. 5. Nitrogen adsorption–desorption isotherm (left) and pore size distribution curves (right) of BW-X-AL samples.

property from the UV light region to the visible light absorption shorter than 450 nm. The steep shape of the spectrum indicates that the visible light absorption is not due to the transition from the impurity level but is due to the band gap transition. The obtained results were similar with previous reports [41,42]. The considerable visible light absorption of BW is attributed to the transition from the hybrid orbital of O 2p and Bi 6s to the W 5d orbital [15]. This observed redshift could be to a charge-transfer transition between the RGO and BW conduction or valance band [43]. For a crystalline semiconductor, it shows that the optical absorption near the band edge follows the equation $ah\nu = A(h\nu - E_g)^{n/2}$, where a , ν , E_g and A are the absorption coefficient, the light frequency, the band gap, and a constant, respectively [44]. According to this equation, the energy of the band gap of pure BW-20-AL is estimated to be the smallest. Therefore, the visible light responses of these RGO/BW series samples are significantly improved by its optimum amount of the RGO doping (BW-20-AL), and thus it should have enhanced photoactivity than those of other samples.

3.6. Photocatalytic performance and sample regeneration

RhB, a widely used dye, was chosen as a representative pollutant to evaluate the photocatalytic performance of photocatalysts. When dissolved in distilled water, RhB shows a major absorption band centered at 553 nm, which was used to monitor the photocatalytic degradation of RhB. Fig. 6 displays the temporal evolution of spectra during the photodegradation of RhB mediated by BW-20-AL under UV and visible light degradation condition. A rapid decrease of RhB absorption at wavelength of 553 nm was observed, accompanied with an absorption band shift to shorter wavelengths. Similar hypsochromic shifts have been observed in the previous reports [45,46]. The sharp decrease and fade of the RhB (Inset) within 40 min indicate the BW-20-AL sample exhibits excellent photocatalytic activity on degradation of the RhB due to its novel flower-like nanostructure and higher specific surface areas. Under visible light irradiation, keeping other conditions constant, Fig. 6b shows the lower degradation efficiency of the BW-20-AL over RhB than under UV irradiation. The main reason is that the energy of the UV-light is much higher than that of the visible light. Meanwhile, Fig. 6b (inset) also indicated that the longer degradation time under visible light was desired than that of UV light.

As shown in Fig. 7, as an overall comparison, RhB degradation without a photocatalyst was also performed, and the results demonstrated that the degradation of RhB was very slow in the absence of photocatalyst or light-off irradiation. However, the removal efficiency of the RGO for RhB is higher than those of the

BW and BW-AL samples. Because the higher BET specific surface area of the RGO could favor the dye-physorption during the light-off period. The obtained results are similar with previous report [33]. And the catalytic efficiency of the P25 is almost same with the unmodified BW samples (BW and BW-AL). The photodegradation efficiency of RhB by BW and BW-AL (Fig. 7A (a and b curves)) only reached about 20% after 40 min reaction. Interestingly, 98%, 80% and 56% of RhB was photocatalytically degraded by the BW-20-AL, BW-30-AL and BW-50-AL samples, respectively. Therefore, the result indicated that BW-20-AL possessed the highest activity. The catalytic efficiencies of the different samples under visible light irradiation possess the similar tendency with the UV light condition (as shown in Fig. 7B).

In order to investigate the generality of the photoactivities for removal of other pollutants, we also carried out the degradation of phenol and Cr(VI) in aqueous solution under UV and visible light irradiation. In all, the results are similar with Fig. 8 that the adsorption performances of the RGO for the phenol and Cr(VI) are better than those of other samples. Fig. 8A–D represents the phenol and Cr(VI) concentration ratio (C_t/C_0) of different samples and those of the direct photolysis process with irradiation time, respectively. Obviously, after irradiation for 80 min, Fig. 8A shows that the highest phenol conversion was 87% over the BW-20-AL. And we can find that the phenol conversion over the as-fabricated catalyst within 80 min of reaction decreased in the order of BW-20-AL > BW-30-AL \approx BW-50-AL > BW-AL \approx BW. Similar results were also observed in the degradation of Cr(VI) under visible light-irradiation within 120 min (Fig. 8B). Comparing with Fig. 8A and C, Fig. 8B and D showed that the rates of the removal of phenol and Cr(VI) were lower, correspondingly.

From the application point of view, the regeneration of a photocatalyst is important and necessary. To investigate the stability of the RGO/BW nanocomposite, we chose the BW-50-AL sample to evaluate the stability and regeneration of the photocatalyst. Before each experiment, the photocatalyst samples used were cleaned through simple ultrasonication and wash. The results of these repeated experiment show that BW-50-AL nanocomposite was very stable (Fig. S4A) since there was only a slight decrease in degradation efficiency over times. The contamination of the surface of the catalyst could be responsible for the phenomenon.

Moreover, we utilized FTIR, XRD and SEM tests to characterize the BW-50-AL after five repeated times. The obtained results were consisted with the previous reports [19,24,25] (Fig. S4B–D). The outcomes proved morphology of the sample unchanged after the photocatalytic process. Above all, the photocatalyst might be

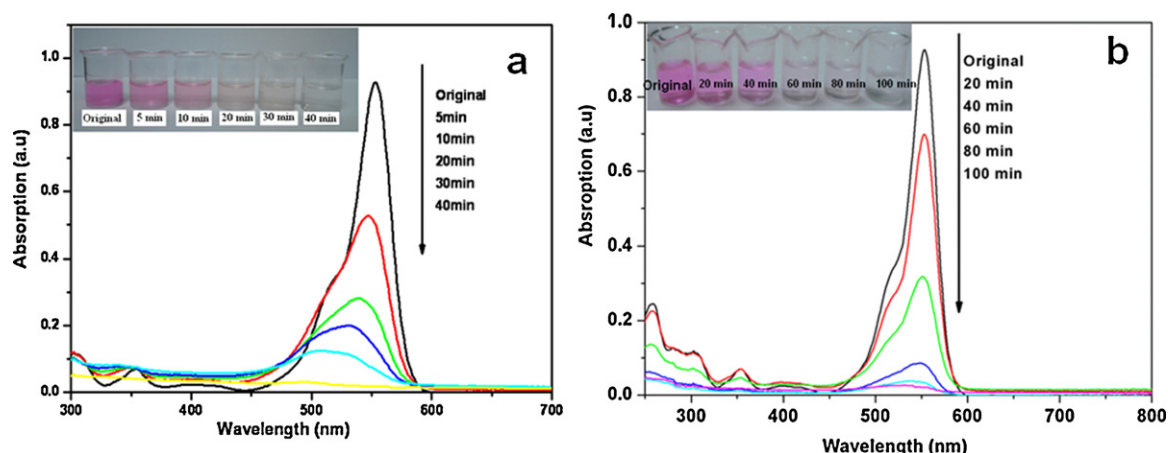


Fig. 6. The temporal evolutions of the spectra during the photodegradation of the RhB mediated by BW-20-AL sample under different light sources: (a) UV and (b) visible light, respectively (Insets show the fade of the RhB).

reused in the industrial aspects owing to its superstable performance.

3.7. Possible mechanism of photocatalytic activity enhancement

It is known that during photocatalysis, the light absorption and charge transfer and separation are crucial factors [27,47–51]. The enhancement of the photocatalytic performance should be ascribed to the increase of the light absorption intensity and range, and the reduction of electron-hole pair recombination in BW in the presence of RGO in the composite, which have been confirmed from the above-mentioned characterizations. Therefore, BW-X-AL samples possess higher activity than those of BW and BW-AL. However, the photocatalytic performance deteriorates, when the RGO content is further increased above its optimum value. Therefore, the order of the catalytic activity: BW-20-AL > BW-30-AL > BW-50-AL. The obtained results are similar with previous report [52]. Such energy levels are beneficial for transfer of photo-induced electrons from the BW conduction band to the RGO, which could efficiently separate the photo-induced electrons and hinder the charge recombination in electron-transfer processes [53,54], enhancing the photocatalytic performance. This phenomenon is ascribed to the following reasons: (i) RGO may absorb some light and thus cause a light harvesting competition between BW and RGO with the increase of the RGO content, which leads to the decrease of the

photocatalytic performance [53,55]. (ii) The excessive RGO can act as a kind of recombination center instead of providing an electron pathway and promote the recombination of electron-hole pairs in RGO [53,56]. (iii) The BW-20-AL sample possesses the highest BET ($37 \text{ m}^2/\text{g}$), which can supply more surface active sites and make the transfer of charge carrier easier, leading to an enhancement of the photocatalytic performance [57].

3.8. Formation mechanism

Generally, the adsorption of additives on certain surfaces plays an important role in the shape-controlled growth for some materials [57]. According to the reports, due to the Van der Waals interaction of surfactant molecules adsorbed on the nanocrystal surfaces and tendency to minimize the interfacial energy, these nanoparticles would gradually self-assemble into aggregations with a specific morphology [58].

From the above-mentioned evidences, the growth mechanism of the as-synthesized products is easily understandable now. A schematic illustration of the growth mechanism is presented in Fig. 9. The initial microcrystal including Bi^{3+} and WO_4^{2-} formed BW nanoparticles in early stage of the reaction system. BW sample was obtained in the absence of the AL and GO under hydrothermal condition. Keeping the experimental conditions constant, the BW-AL was fabricated by using AL as a “soft” template to form BW-AL

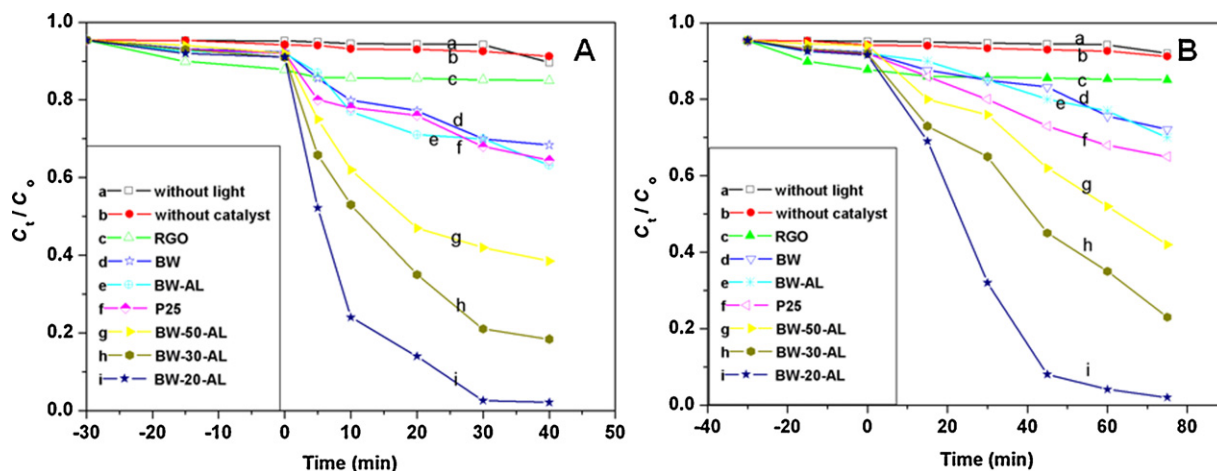


Fig. 7. Comparisons of the photocatalytic degradation of RhB in the presence of the (a) without light; (b) without catalyst; (c) RGO; (d) BW; (e) BW-AL; (f) P25; (g) BW-30-AL; (h) BW-50-AL; and (i) BW-20-AL.

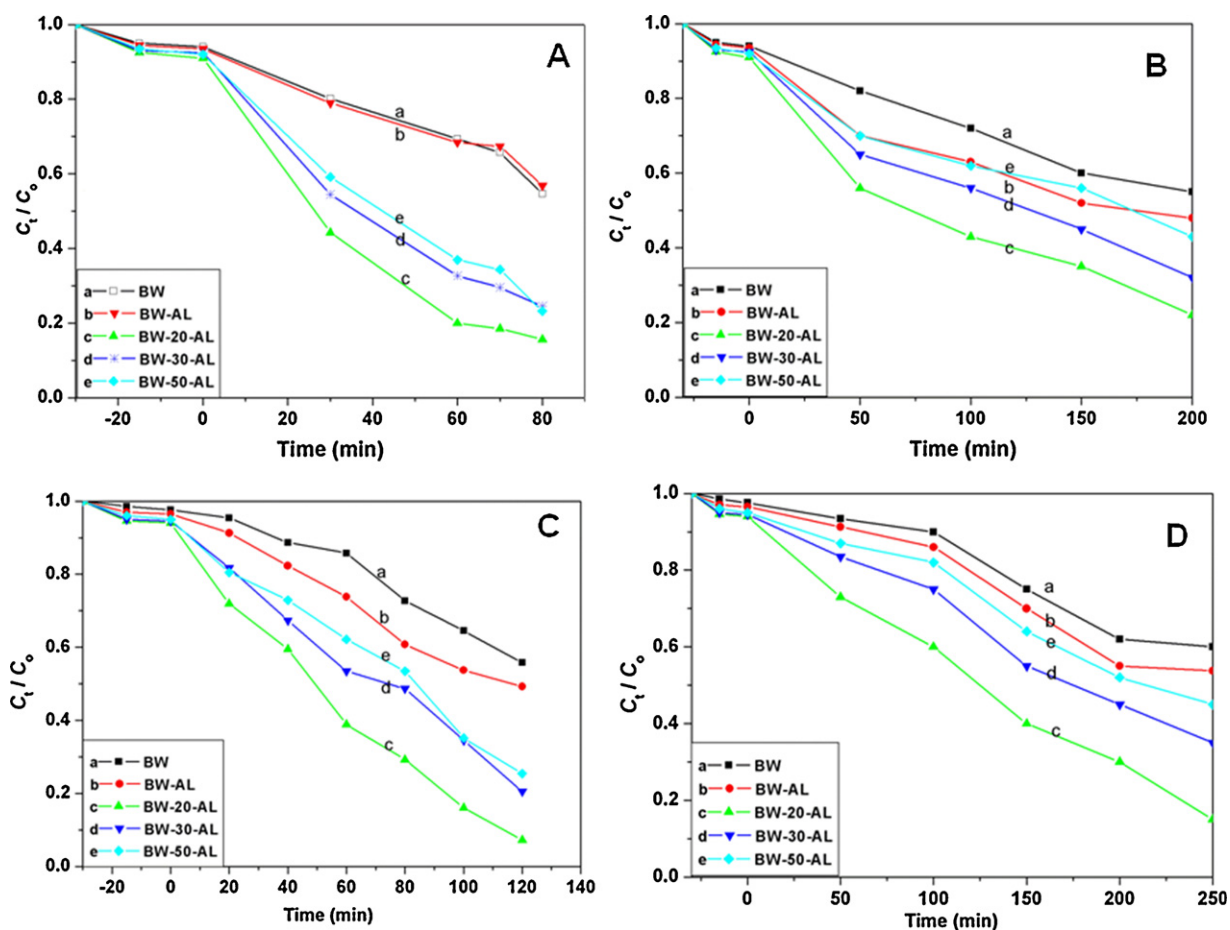


Fig. 8. Degradation curves under different conditions by the samples for (A: (UV irradiation) and B: (Visible light)) phenol; (C: (UV irradiation) and D: (Visible light)): Cr (VI).

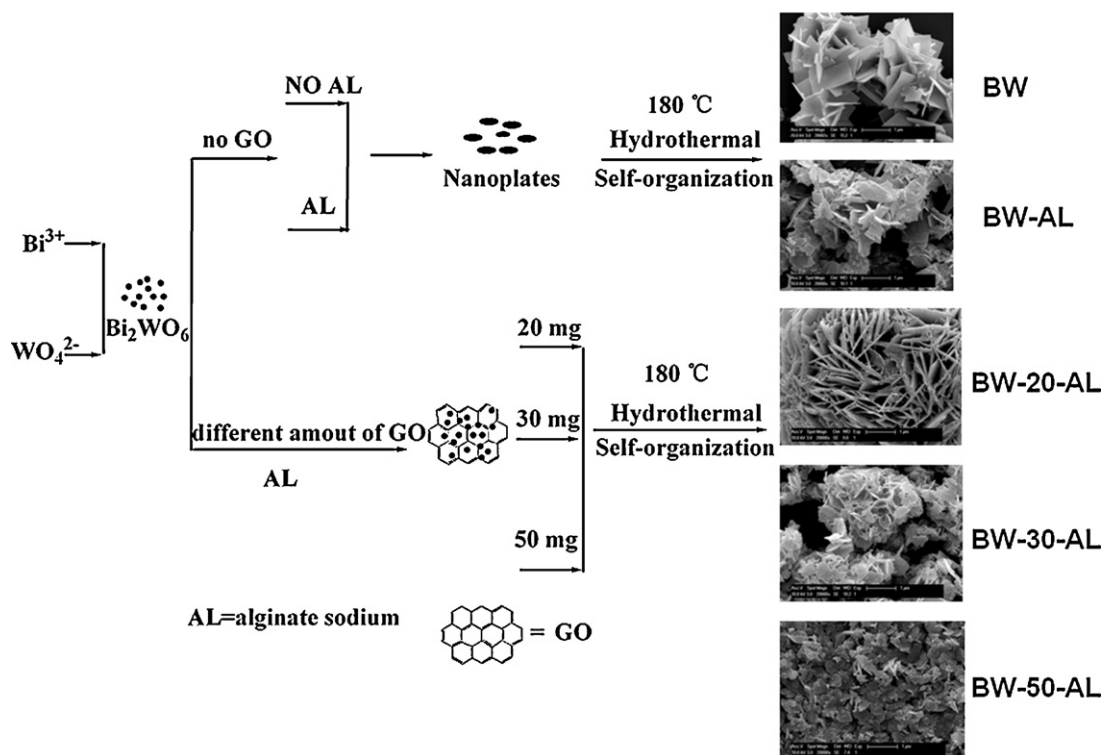


Fig. 9. Formation process for different products obtained under different conditions.

sample. On the other hand, in the co-presence of GO and AL, the GO was reduced to RGO by the AL. So, the BW-X-AL nanocomposites were obtained with the different amount of GO. As shown in Fig. 9, the flower-like microsphere formed (BW-20-AL), when 20 mg GO was added to the solution. With the amount of the GO increasing to 30 mg, more RGO nanosheets acted as structure-directing agent to fabricate the BW-30-AL nanocomposite. Therefore, the morphology of the BW-30-AL changed from the flower-like sphere to the broken sphere nanostructures. Finally, when the amount of the GO reached 50 mg, the sphere collapsed completely owing to the more amount of GO.

4. Conclusions

With $\text{Bi}(\text{NO}_3)_3 \cdot 6\text{H}_2\text{O}$ and $\text{Na}_2\text{WO}_4 \cdot 2\text{H}_2\text{O}$ as inorganic metal source, AL as reducing agent, and in the absence or presence of GO, BW and BW-X-AL with various morphologies could be selectively prepared via a facile hydrothermal route under different conditions. It is shown that the amount of the GO greatly influenced the morphologies, and even crystalline structure of the product. The appropriate amount RGO modified BW can significantly promote the performance for degradation of RhB as well as phenol and Cr(VI) pollutants. Moreover, RGO facilitates the transfer of photogenerated electrons to model materials, leading to significant improvement in the photocatalytic performance. More importantly, the as-obtained photocatalyst could be regenerated after simple ultrasonication and simple washing. Our work may open up a new avenue toward the photocatalytic activity of BW and other hybrid nanomaterials, which can meet the growing demands for environmental purification from industrial effluents.

Appendix A. Supplementary data

Supplementary data associated with this article can be found, in the online version, at <http://dx.doi.org/10.1016/j.apcatb.2012.03.023>.

References

- [1] W.X. Zhang, J.C. Cui, C.A. Tao, Y.G. Wu, Z.P. Li, L. Ma, Y.Q. Wen, G.T. Li, *Angewandte Chemie International Edition* 48 (2009) 5864–5868.
- [2] D. Li, M.B. Müller, S. Gilje, R.B. Kaner, G.G. Wallace, *Nature Nanotechnology* 3 (2008) 101–105.
- [3] Y.X. Huang, X.W. Liu, J.F. Xie, G.P. Sheng, G.Y. Wang, Y.Y. Zhang, A.W. Xu, H.Q. Yu, *Chemical Communications* 47 (2011) 5795–5797.
- [4] X. Wang, L.J. Zhi, K. Müllen, *Nano Letters* 8 (2008) 323–327.
- [5] K.S. Novoselov, D. Jiang, F. Schedin, T.J. Booth, V.V. Khotkevich, S.V. Morozov, A.K. Geim, *Proceedings of the National Academy of Sciences of the United States of America* 102 (2005) 10451–10453.
- [6] H.C. Schniepp, J.L. Li, M.J. McAllister, H. Sai, M. Herrera-Alonso, D.H. Adamson, R.K. Prud'homme, R. Car, D.A. Saville, I.A. Aksay, *Journal of Physical Chemistry B* 110 (2006) 8535–8539.
- [7] Z.B. Lei, L. Lu, X.S. Zhao, *Energy & Environmental Science* 4 (2011) 4009–4015.
- [8] W.S. Hummers, R.E. Offeman, *Journal of the American Chemical Society* 80 (1958) 1339.
- [9] S. Stankovich, D.A. Dikin, R.D. Piner, K.A. Kohlhaas, A. Kleinhammes, Y. Jia, Y. Wu, S.T. Nguyen, R.S. Ruoff, *Carbon* 45 (2007) 1558–1565.
- [10] Y.X. Zhou, H.B. Yao, Q. Zhang, J.Y. Gong, S.J. Liu, S.H. Yu, *Inorganic Chemistry* 48 (2009) 1082–1090.
- [11] X.F. Cao, L. Zhang, X.T. Chen, Z.L. Xue, *CrystEngComm* 13 (2011) 306–311.
- [12] Y.H. Shi, S.H. Feng, C.S. Cao, *Materials Letters* 44 (2000) 215–218.
- [13] N.A. McDowell, K.S. Knight, P. Lightfoot, *Chemistry—A European Journal* 12 (2006) 1493–1499.
- [14] H.B. Fu, C.S. Pan, W.Q. Yan, Y.F. Zhu, *Journal of Physical Chemistry B* 109 (2005) 22432–22439.
- [15] C. Zhang, Y.F. Zhu, *Chemistry of Materials* 17 (2005) 3537–3545.
- [16] D.K. Ma, S.M. Huang, W.X. Chen, S.W. Hu, F.F. Shi, K.L. Fan, *Journal of Physical Chemistry C* 113 (2009) 4369–4374.
- [17] M. Shang, W.Z. Wang, J. Ren, S.M. Sun, L. Wang, L. Zhang, *Journal of Materials Chemistry* 19 (2009) 6213–6218.
- [18] F. Amano, K. Nogami, M. Tanaka, B. Ohtani, *Langmuir* 26 (2010) 7174–7180.
- [19] G.K. Zhang, F. Lü, M. Li, J.L. Yang, X.Y. Zhang, B.B. Huang, *Journal of Physics and Chemistry of Solids* 71 (2010) 579–582.
- [20] L.S. Zhang, W.Z. Wang, Z.G. Chen, *Journal of Materials Chemistry* 17 (2007) 2526–2532.
- [21] L.S. Zhang, W.Z. Wang, L. Zhou, H.L. Xu, *Small* 3 (2007) 1618–1625.
- [22] J. Wu, F. Duan, Y. Zheng, Y. Xie, *Journal of Physical Chemistry C* 111 (2007) 12866–12871.
- [23] Y.Y. Li, J.P. Liu, X.T. Huang, G.G. Li, *Crystal Growth and Design* 7 (2007) 1350–1355.
- [24] Y.Y. Li, J.G. Liu, X.T. Huang, *Nanoscale Research Letters* 3 (2008) 365–371.
- [25] Y.Y. Li, J.P. Liu, X.T. Huang, J.G. Yu, *Dalton Transactions* 39 (2010) 3420–3425.
- [26] M. Shang, W.Z. Wang, L. Zhang, H.L. Xu, *Materials Chemistry and Physics* 120 (2010) 155–159.
- [27] E.P. Gao, W.Z. Wang, M. Shang, J.H. Xu, *Physical Chemistry Chemical Physics* 13 (2011) 2887–2893.
- [28] A. Kongkanand, R.M. Domínguez, P.V. Kamat, *Nano Letters* 7 (2007) 676–680.
- [29] D.M. Guldí, G.M.A. Rahman, V. Sgobba, N.A. Kotov, D. Bonifazi, M. Prato, *Journal of the American Chemical Society* 128 (2006) 2315–2323.
- [30] B. Farrow, P.V. Kamat, *Journal of the American Chemical Society* 131 (2009) 11124–11131.
- [31] J.F. Shen, N. Li, M. Shi, Y.Z. Hu, M.X. Ye, *Journal of Colloid and Interface Science* 348 (2010) 377–383.
- [32] J.F. Shen, Y.Z. Hu, C. Li, C. Qin, M.X. Ye, *Small* 5 (2009) 82–85.
- [33] Y.L. Min, K. Zhang, Y.C. Chen, Y.G. Zhang, *Separation and Purification Technology* 86 (2012) 98–105.
- [34] G. Williams, B. Seger, P.V. Kamat, *ACS Nano* 2 (2008) 1487–1491.
- [35] J. Li, C.Y. Lin, *European Journal of Inorganic Chemistry* 10 (2012) 1244–1248.
- [36] H.X. Chang, Z.H. Sun, Z.H. Sun, K.Y. Fong Ho, X.M. Ting, F. Yan, W.M. Kwok, Z.J. Zhen, *Nanoscale* 3 (2011) 258–264.
- [37] M. Crane, R. Frost, P. Williams, T. Klopogge, *Journal of Raman Spectroscopy* 33 (2002) 62–66.
- [38] S. Guo, D. Wen, Y. Zhai, S. Dong, E. Wang, *ACS Nano* 4 (2010) 3959–3968.
- [39] T.N. Lambert, C.A. Chavez, B. Hernandez-Sanchez, P. Liu, N.S. Bell, A. Ambrosini, T. Fredman, T.J. Boyle, D.R. Wheeler, D.L. Huber, *Journal of Physical Chemistry C* 113 (2009) 19812–19823.
- [40] G. Dong, L.Z. Zhang, *Journal of Materials Chemistry* 22 (2012) 1160–1166.
- [41] F. Duan, Y. Zhang, M.Q. Chen, *Applied Surface Science* 257 (2011) 1972–1978.
- [42] A. Kudo, I. Tsuji, H. Kato, *Chemical Communications* 17 (2002) 1958–1959.
- [43] F. Li, X. Li, M. Hou, K. Cheah, W. Choy, *Applied Catalysis A-General* 285 (2005) 181–189.
- [44] M. Arslan, H. Duymus, F. Yakuphanoglu, *Journal of Physical Chemistry B* 110 (2006) 276–280.
- [45] L.S. Zhang, W.Z. Wang, Z.G. Chen, L. Zhou, H.L. Xu, W. Zhu, *Journal of Materials Chemistry* 17 (2007) 2526–2532.
- [46] W. Zhao, C. Chen, X. Li, J. Zhao, *Journal of Physical Chemistry B* 106 (2002) 5022–5028.
- [47] J.Q. Yu, A. Kudo, *Advanced Functional Materials* 16 (2006) 2163–2169.
- [48] D.L. Liao, B.Q. Liao, *Journal of Photochemistry and Photobiology A* 187 (2007) 363–369.
- [49] J.S. Valente, F. Tzompantzi, J. Prince, J.G.H. Cortez, R. Gomez, *Applied Catalysis B* 90 (2009) 14916–14921.
- [50] H.Y. Jiang, H.X. Dai, X. Meng, K.M. Ji, L. Zhang, J.G. Deng, *Applied Catalysis B* 105 (2011) 326–334.
- [51] H. Zhang, X.J. Lv, Y.M. Li, Y. Wang, J.H. Li, *ACS Nano* 4 (2010) 380–386.
- [52] X.J. Liu, L.K. Pan, T. Lv, G. Zhu, T. Lu, Z. Sun, C.Q. Sun, *Chemical Communications* 47 (2011) 11984–11986.
- [53] Q. Lin, B.D. Guo, J.G. Yu, J.R. Ran, B.H. Zhang, H.J. Yan, J.R. Gong, *Journal of the American Chemical Society* 133 (2011) 10878–10884.
- [54] G. Zhu, T. Xu, T. Lv, L.K. Pan, Q.F. Zhao, Z. Sun, *Journal of Electroanalytical Chemistry* 650 (2011) 248–251.
- [55] Y.B. Tang, C.S. Lee, J. Xu, Z.T. Liu, Z.H. Chen, Z.B. He, Y.L. Cao, G.D. Yuan, H.S. Song, L.M. Chen, L.B. Luo, H.M. Cheng, W.J. Zhang, I. Bello, S.T. Lee, *ACS Nano* 4 (2010) 3482–3488.
- [56] N.L. Yang, J. Zhai, D. Wang, Y.S. Chen, L. Jiang, *ACS Nano* 4 (2010) 887–894.
- [57] X.G. Peng, L. Manna, W.D. Yang, J. Wickham, E. Scher, A. Kadavanich, A.P. Alivisatos, *Nature* 404 (2000) 59–61.
- [58] F. Bai, D.S. Wang, Z.Y. Huo, W. Chen, L.P. Liu, X. Liang, C. Chen, X. Wang, Q. Peng, Y.D. Li, *Angewandte Chemie International Edition* 46 (2007) 6650–6653.